Fuel Droplet Evaporation in a Supercritical Environment

G. S. Zhu[1]

S. K. Aggarwal[2]

Department of Mechanical Engineering,
University of Illinois at Chicago,
Mail Code 251,
Chicago, IL 60607-7022

This paper reports a numerical investigation of the transcritical droplet vaporization phenomena. The simulation is based on the time-dependent conservation equations for liquid and gas phases, pressure-dependent variable thermophysical properties, and a detailed treatment of liquid-vapor phase equilibrium at the droplet surface. The numerical solution of the two-phase equations employs an arbitrary Eulerian-Lagrangian, explicit-implicit method with a dynamically adaptive mesh. Three different equations of state (EOS), namely the Redlich-Kwong (RK), the Peng-Robinson (PR), and Soave-Redlich-Kwong (SRK) EOS, are employed to represent phase equilibrium at the droplet surface. In addition, two different methods are used to determine the liquid density. Results indicate that the predictions of RK-EOS are significantly different from those obtained by using the RK-EOS and SRK-EOS. For the phase-equilibrium of n-heptane-nitrogen system, the RK-EOS predicts higher liquid-phase solubility of nitrogen, higher fuel vapor concentration, lower critical-mixing-state temperature, and lower enthalpy of vaporization. As a consequence, it significantly overpredicts droplet vaporization rates, and underpredicts droplet lifetimes compared to those predicted by PR and SRK-EOS. In contrast, predictions using the PR-EOS and SRK-EOS show excellent agreement with each other and with experimental data over a wide range of conditions. A detailed investigation of the transcritical droplet vaporization phenomena indicates that at low to moderate ambient temperatures, the droplet lifetime first increases and then decreases as the ambient pressure is increased. At high ambient temperatures, however, the droplet lifetime decreases monotonically with pressure. This behavior is in accord with the reported experimental data. [DOI: 10.1115/1.1385198]

Introduction

Droplet gasification in high-pressure environments, where the thermodynamic conditions correspond to the supercritical state of the liquid fuel, is important in diesel engines, liquid rockets, and gas turbine combustors. In jet engines used in military applications, the liquid fuel is the primary coolant for on-board heat sources, and may attain a critical state before it is ''atomized.'' The gas turbine combustors used in propulsion applications are being designed to operate at increasingly higher pressures, which may exceed the critical pressure of the fuel. The modeling of transcritical droplet vaporization also represents a scientifically challenging problem, since the conventional ''low-pressure'' droplet models are generally not valid at high-pressure conditions. For example, the gas-phase nonidealities and the liquid-phase solubility of gases are negligible at low pressures, but become essential considerations at high pressures. Consequently, a single-component fuel droplet would assume a multicomponent behavior, and liquid mass transport in the droplet interior would become an important process. Secondly, as the droplet surface approaches the transcritical state, the latent heat reduces to zero, and the gas and liquid densities become equal at the droplet surface. Then, transient effects in the gas phase would become as important as those in the liquid phase, since the characteristic times for transport processes in the two phases become comparable. In addition, the liquid and gas-phase thermophysical properties become pressure-dependent. Also, under convective conditions, the droplet distortion and breakup become important processes, as the surface tension is greatly diminished and approaches zero at the critical point.

Due to its significant practical and fundamental relevance, the supercritical droplet gasification phenomena has been a subject of many theoretical and experimental investigations. Manrique and Borman [1] presented a methodology to consider several high-pressure effects in a quasi-steady model that was based on the Redlich-Kwong (RK-EOS) equation of state ([2]). In a subsequent study ([3]), it was demonstrated that the effects due to thermodynamic nondealities and property variations modified the vaporization behavior significantly. Lazar and Faeth [4] and Canada and Faeth [5] also employed RK-EOS to develop a high-pressure model to investigate steady-state droplet vaporization and combustion for hydrocarbon fuels. They found the droplet burning-rate predictions of the high-pressure model to be similar to those of a conventional low-pressure model. In addition, the results of both models were in fair agreement with their experimental data. Matlosz et al. [6] developed a high-pressure model in which the gas-phase unsteadiness and real gas effects were included, while the gas absorption in liquid droplet was neglected.

Curtis and Farrell [7,8] developed a high-pressure model, using the Peng-Robinson (PR-EOS) equation of state ([9]) that predicted the droplet vaporization rate, temperature, and the critical mixing state. It was shown that for droplet vaporization under conditions similar to those in diesel engines, the anomalies in transport properties near the critical mixing state were insignificant. Hsieh et al. [10] reported a comprehensive analysis of the high-pressure droplet vaporization phenomena in binary and ternary systems at a temperature of 2000 K. The Soave-Redlich-Kwong equation of state (SRK-EOS) ([11]) was employed in the analysis. In a subsequent study, Shuen et al. [12] extended their high-pressure model to examine the combustion behavior of an n-pentane droplet under subcritical and supercritical conditions. Their results indicated a continuous increase in the droplet gasification rate with pressure, with a more rapid increment occurring near the critical burning pressure of the fuel. Delpanque and Sirignano [13] also

[1]Currently at the University of Wisconsin at Madison.

[2]To whom all correspondence should be addressed.

Contributed by the International Gas Turbine Institute (IGTI) of THE AMERICAN SOCIETY OF MECHANICAL ENGINEERS for publication in the ASME JOURNAL OF ENGINEERING FOR GAS TURBINES AND POWER. Paper presented at the International Gas Turbine and Aeroengine Congress and Exhibition, Indianapolis, IN, June 7–10, 1999; ASME Paper 99-GT-301. Manuscript received by IGTI, March 1999; final revision received by the ASME Headquarters, August 2000. Associate Editor: H. D. Nelson.

considered a transient, spherically symmetric model to investigate transient gasification of a liquid oxygen droplet in gaseous hydrogen at high pressures. It was noted that at supercritical pressures, the droplet surface temperature reaches the critical mixing value. Jia and Gogos [14,15] employed the PR-EOS to quantify the effect of liquid-phase gas solubility on the vaporization of an n-hexane droplet for a range of ambient pressures and temperatures. The variation of droplet lifetime with pressure was shown to exhibit a maximum at low ambient temperatures, but to decrease monotonically with pressure at high ambient temperatures. Stengel et al. [16] employed the SRK-EOS to examine the vaporization behavior of freely falling n-heptane droplets in a nitrogen environment. Results from a quasi-steady droplet model were compared with measurements for ambient pressure up to 40 atm. Aggarwal et al. [17] also reported a quasi-steady high-pressure model that used the PR-EOS and considered the thermophysical properties to be pressure-dependent. The transient liquid-phase processes were also included in the model. The computed vaporization histories were shown to compare well with the measurements of Stengel et al. [16].

An important result from several numerical and experimental investigations ([18–21]) is that a droplet does not immediately attain the critical mixing state as it is introduced into an ambient where the pressure and temperature exceed the thermodynamic critical point of the liquid fuel. Also, while most studies indicate that the droplet surface generally reaches the critical mixing state at some pressure that is much higher than the fuel critical pressure, they report a wide scatter in the minimum ambient pressure required for the attainment of the critical state. The literature review also indicates that several different EOS have been employed to represent the liquid-vapor phase equilibrium at the droplet surface. Clearly, an accurate representation of phase equilibrium is essential for a realistic simulation of droplet evaporation at high pressures. Previous studies have not examined in detail the accuracy of various EOS and their effects on the predicted transcritical/supercritical droplet vaporization behavior. The present study is motivated by these considerations.

In the present study, a comprehensive model is developed to investigate the transcritical droplet vaporization phenomena. The model is first used to examine the effects of different EOS on the prediction of phase equilibrium for an n-heptane-nitrogen system, as well as on the prediction of droplet gasification rate in a supercritical environment. A detailed numerical study is then conducted to characterize the transcritical vaporization phenomena, including the transition from subcritical to supercritical state, and the subsequent supercritical droplet gasification behavior.

Problem Formulation

The physical problem described here considers the transient gas and liquid-phase processes associated with an isolated fuel droplet. The droplet, which is initially at a subcritical state, is suddenly introduced into a stagnant gas environment with its thermodynamic state in the supercritical regime of the fuel species. In the following, we describe the transient two-phase governing equations in a spherical coordinate system, along with the interphase conditions at the droplet surface.

For the gas-phase region, $r>r_s(t)$, the governing equations include the conservation equations for species, momentum, energy, and the equation of state (EOS):

$$\frac{\partial \rho_k}{\partial t}+\frac{1}{r^2}\frac{\partial}{\partial r}(\rho_k u r^2)=\frac{1}{r^2}\frac{\partial}{\partial r}\left[\rho D_k r^2 \frac{\partial}{\partial r}\left(\frac{\rho_k}{\rho}\right)\right] \tag{1}$$

$$\frac{\partial \rho u}{\partial t}+\frac{1}{r^2}\frac{\partial}{\partial r}(\rho u^2 r^2)+\frac{\partial p}{\partial r}=\frac{1}{r^2}\frac{\partial}{\partial r}\left[2\mu r^2\frac{\partial u}{\partial r}+\lambda\frac{\partial}{\partial r}(ur^2)\right]-\frac{2}{r^2}\left[2\mu u+\frac{\lambda}{r}\frac{\partial}{\partial r}(ur^2)\right] \tag{2}$$

$$\frac{\partial \rho I}{\partial t}+\frac{1}{r^2}\frac{\partial}{\partial r}(\rho I u r^2)+\frac{p}{r^2}\frac{\partial}{\partial r}(ur^2)=\frac{1}{r^2}\left\{\frac{\partial}{\partial r}r^2\rho D_k\left[\sum_{k=1}^{N}h_k\frac{\partial}{\partial r}\left(\frac{\rho_k}{\rho}\right)\right]\right\}+\frac{1}{r^2}\frac{\partial}{\partial r^2}\left(kr^2\frac{\partial T}{\partial r}\right)+\frac{\partial u}{\partial r}\left[2\mu\frac{\partial u}{\partial r}+\frac{\lambda}{r^2}\frac{\partial}{\partial r}(ur^2)\right]+\frac{2u}{r^2}\left[2\mu u+\frac{\lambda}{r}\frac{\partial}{\partial r}(ur^2)\right] \tag{3}$$

$$f_1(p,T,\rho_1,\rho_2,\ldots,\rho_N)=0. \tag{4}$$

In the above equations, D_k, ρ_k, and h_k are, respectively, the diffusion coefficient, density, and specific enthalpy of kth species. N is the total number of species. Further, k, μ, and λ are the thermal conductivity, viscosity, and second viscosity coefficient, respectively. Equation (4) represents a P-V-T relation for the fluid mixture. A cubic EOS is employed, which can be written in a general form as ([22])

$$p=\frac{RT}{V-b}-\frac{a}{V^2+ubV+wb^2} \tag{5}$$

where a and b are functions of temperature and species mole fractions. u and w are constants. Their values are: $u=2$, $w=-1$ for PR-EOS; and $u=1$, $w=0$ for SRK-EOS and RK-EOS.

For the liquid-phase region, $r<r_s$, the governing equations for the liquid temperature and species mass fractions are

$$\frac{\partial}{\partial t}(\rho_l C_{pl} T_l)=\frac{1}{r^2}\frac{\partial}{\partial r}\left(k_l r^2\frac{\partial T_l}{\partial r}\right)+\frac{1}{r^2}\frac{\partial}{\partial r}\left[r^2\sum_{k=1}^{N}\rho_l D_l h_k\frac{\partial}{\partial r}\left(\frac{\rho_{lk}}{\rho_l}\right)\right] \tag{6}$$

$$\frac{\partial \rho_{lk}}{\partial t}=\frac{1}{r^2}\frac{\partial}{\partial r}\left[\rho_{lk}D_l r^2\frac{\partial}{\partial r}\left(\frac{\rho_{lk}}{\rho_l}\right)\right]. \tag{7}$$

Boundary Conditions

The boundary conditions at the droplet center ($r=0$) are: $\partial T_l/\partial r=0$ and $\partial \rho_k/\partial r=$, and those at $r\to\infty$ are: $T\to T_\infty$, $p\to p_\infty$, and $\rho_k\to\rho_{k\infty}$. At the droplet surface, $r=r_s$, the condition of mass and energy conservation, and thermodynamic equilibrium are

$$\dot{m}X_k-\rho_{lk}D_l\left.\frac{\partial X_k}{\partial r}\right|_{r=r_s^-}=\dot{m}Y_k-\rho_k D_k\left.\frac{\partial Y_k}{\partial r}\right|_{r=r_s^+} \tag{8}$$

$$-k_l\left.\frac{\partial T_l}{\partial r}\right|_{r=r_s^-}=-k\left.\frac{\partial T}{\partial r}\right|_{r=r_s^+}+\sum_{k=1}^{N}\left(\dot{m}Y_k-\rho_k D_k\frac{\partial Y_k}{\partial r}\right)\Bigg|_{r=r_s'}\Delta H_{vk}+\dot{m}\left[\frac{u^2}{2}-u\frac{dr_s}{dt}-\frac{1}{\rho}\left(2\mu\frac{\partial u}{\partial r}+\frac{\lambda}{r^2}+\frac{\partial}{r^2}\frac{\partial}{\partial r}(ur^2)\right)\right] \tag{9}$$

$$f_2(T_s,P_s,X_{1s},X_{2s},\ldots,X_{Ns},Y_{1s},Y_{2s},\ldots,Y_{Ns})=0 \tag{10}$$

where X_{is} and Y_{is} represent, respectively, the liquid and gas-phase mole fractions of ith species at the droplet surface. The specific form of Eq. (10) can be derived from the condition of thermodynamic and mechanical equilibrium at the droplet surface. At low pressures, the equilibrium is normally expressed by the Raoult's law. At elevated pressures, however, it should be described from a more general thermodynamic consideration, as discussed in the next section.

In a supercritical environment, depending on the ambient and droplet properties, the droplet may experience a thermodynamic

state transition from subcritical to supercritical. Equations (8)–(10) are only applicable until the droplet surface reaches a critical mixing point. The subsequent droplet regression is then characterized by the motion of the critical surface which moves inward continuously.

Vapor-Liquid Equilibrium at the Drop Surface

The vapor-liquid equilibrium at the droplet surface is represented by the equality of temperature and pressure, and the fugacity of each species in the gas and liquid phases. The equality of fugacity of species k is expressed as

$$\phi_k^v Y_k = \phi_k^l X_k \tag{11}$$

where the superscripts v and l refer to the vapor and liquid phase, respectively. ϕ_k is a function of pressure, temperature, and composition. It is given by the following relation:

$$RT\ln(\phi_k) = \int_v^\infty \left[\left(\frac{\partial P}{\partial n_k} \right)_{T,v,n_j} - \frac{RT}{v} \right] dv - RT\ln z \tag{12}$$

where n_j is the mole number of jth species. By substituting the equation of state (5) into Eq. (12), the fugacity of the kth species in the liquid and gas phase mixture is given by ([22]):

$$\ln\phi_k = \frac{b_k}{b}(z-1) - \ln(z-B) + \frac{A}{B\sqrt{u^2-4w}} \left(\frac{b_k}{b} - \delta_k \right) \times \ln \frac{2Z + B(u+\sqrt{u^2-4w})}{2Z + B(u-\sqrt{u^2-4w})} \tag{13}$$

where

$$\frac{b_k}{b} = \frac{T_{ck}/P_{ck}}{\sum_j y_j T_{cj}/P_{cj}} \quad \text{and}$$

$$\delta_k = \frac{2\sqrt{a_k}}{a} \sum x_j \sqrt{a_j}(1-k_{kj}).$$

The binary interaction coefficient k_{kj} in the above equation is taken from Knapp et al. [23]. It is 0.1441 for PR-EOS, and 0.1422 for SRK and RK-EOS. Equations (11)–(13) provide the basic relations for vapor-liquid equilibrium calculation. These equations along with Eqs. (8)–(9) provide a closed system to determine the temperature and species mole fractions at the droplet surface. It represents a system of highly nonlinear algebraic equations that need to be solved iteratively at each time-step.

For a multicomponent mixture, the latent heat of vaporization of each species is defined as the difference between the partial molar enthalpy of that species in the vapor and liquid phases. The following thermodynamic relation then gives the partial molar enthalpy of kth species:

$$\overline{H}_k - \overline{H}_k^0 = -RT^2 \frac{\partial}{\partial T}(\ln\phi_k) \tag{14}$$

where the superscript 0 denotes the quantity in an ideal state. Equation (14) is solved iteratively along with Eqs. (8)–(9) and (11)–(13).

Thermophysical Properties

The gas and liquid-phase thermo-transport properties are considered function of pressure, temperature, and composition. The method suggested by Chung et al. [24] is employed to calculate the thermal conductivity and viscosity of the gas mixture at high pressures. The binary mass diffusivity is calculated by using the Chapman-Enskog theory in conjunction with the collision integrals given by Neufeld et al. ([25]). It is then corrected for pressure effects by using the Takahashi correlation ([26]). For a multicomponent mixture, the effective diffusivity is obtained by using the formula given by Bird et al. [27]. The gas density is calculated directly from the EOS employed. For the enthalpy of gas mixture, the enthalpy of pure components is obtained from JANAF tables. A generalized thermodynamic correlation based on three-parameter corresponding states ([28]) is then used to calculate the enthalpy correction for high-pressure effects. Then, the specific internal energy of gas mixture in Eq. (3) is given by

$$l = \sum_{k=1}^{N} \frac{\rho_k}{\rho} h_k(T) - \frac{P}{\rho} \tag{15}$$

which relates the energy Eq. (3) to the equation of state (4) through the gas temperature.

The heat capacity of pure liquid components is calculated by a fourth-order polynomial of temperature, and then extended to liquid mixture using the mixture rule of Filippov [29]. The liquid mass diffusivity and thermal conductivity are obtained by using the correlations of Nakanishi [30] and Chung [24] respectively. In the present study, two different methods are employed to determine the liquid density. In the first, the liquid density is obtained directly from the EOS employed, while in the second, it is calculated by using the formulas suggested by Hankinson and Thomson [31] along with the high-pressure correction given by Thomson et al. [32].

Numerical Method

An arbitrary Lagrangian-Eulerian numerical method with a dynamically adaptive mesh is used to solve the governing equations. The solution procedure is as follows: (i) calculate explicitly the contributions of the diffusion and source terms in the gas-phase equations; (ii) calculate implicitly the terms associated with the acoustic pressure in the gas-phase equations; (iii) compute new mesh distribution with the adaptive mesh method, and then the convection terms in the gas-phase equations; and (iv) based on the solutions of above steps, solve implicitly the gas-phase equations, along with the liquid-phase equations as well as the droplet surface and vapor-liquid equilibrium equations.

The adaptive mesh technique is very effective in improving the calculation efficiency. For the supercritical vaporization calculations here, the results show that the minimum number of grid points required to get a grid-independent solution is about 600 for a uniform grid. However, using the adaptive mesh technique, the number of grid points is reduced to 180. A variable time-step is employed. It is calculated automatically based on the stability restrictions of explicit convection and diffusion processes.

Results and Discussion

The present simulations consider an n-heptane droplet evaporating in a high-pressure nitrogen environment. The first set of results focuses on a comparison of the thermodynamic phase equilibrium obtained by using the PR, SRK, and RK-EOS. Figure 1 shows a comparison of the phase-equilibrium predictions of PR, SRK, and RK-EOS at four different pressures. An important observation is that PR and SRK-EOS predict essentially the same equilibrium composition, including the fuel vapor mole fraction and the liquid-phase solubility of nitrogen, over a wide pressure range. In contrast, the predictions of RK-EOS exhibit significant differences from those of PR and SRK-EOS. In both the subcritical and supercritical regimes, the RK-EOS predicts higher fuel vapor mole fraction, which implies that it would yield higher droplet gasification rate compared to that using the PR and SRK-EOS. In addition, the RK-EOS predicts higher liquid-phase solubility of nitrogen in the supercritical regime ($P_r > 1.0$). The critical mixing point obtained by using RK-EOS is also different from that using the other two EOS. The temperatures at the critical

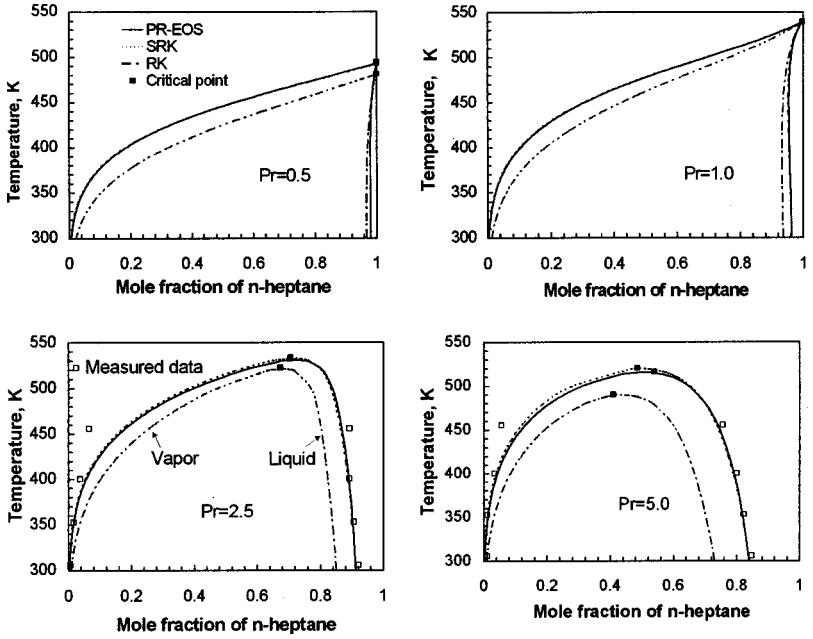

Fig. 1 Mole fraction of n-heptane predicted by PR, SRK, and RK-EOS for an n-heptane-nitrogen system in thermodynamic equilibrium at four different pressures. P_r is the reduced pressure normalized by the critical pressure of pure n-heptane. The experimental data from Chung et al. [23], for $P_r=2.5$ and 5.0, are also included in the plots.

mixing point predicted by RK-EOS are 1.9 and 8.4 percent lower than those predicted by the other two EOS at Pr=2.5 and 5.0, respectively. In addition, results for Pr=2.5 and 5.0 indicate that while the phase-equilibrium predictions of PR and SRK-EOS show good agreement with the experimental data [23] those of RK-EOS show significant differences.

Another important observation from Fig. 1 deals with the solubility of nitrogen into liquid at different ambient pressures and temperatures. At supercritical pressures, the amount of gas absorbed in liquid becomes significant, and increases as the ambient temperature and pressure are increased. This implies that in supercritical environments, the liquid mass transport becomes important and a pure fuel droplet exhibits multicomponent behavior. Also notable in Fig. 1 is that the critical mixing temperature (defined by the critical mixing point) decreases as the pressure is increased. This is indicated more clearly in Fig. 2(*a*), which shows the pressure-temperature diagram for an n-heptane-nitrogen system in equilibrium. Again, the difference between the prediction of RK-EOS and those of SRK and RK-EOS at supercritical pressures is significant. Figure 2(*b*) shows the variation of latent heat of vaporization of n-heptane with temperature as predicted by PR, SRK, and RK-EOS. The heat of vaporization decreases as the temperature and/or pressure is increased, and drops to zero at the critical point. The predictions of PR and SRK-EOS are again in good agreement with each other, while those of RK-EOS exhibit noticeable differences, with RK-EOS underpredicting the heat of vaporization significantly. Clearly, this has important implications for predicting the droplet vaporization rate at supercritical conditions using different EOS.

We now focus on the transient vaporization behavior of an n-heptane droplet which at time $t=0$ is introduced into a high-pressure nitrogen environment. Figure 3 shows the droplet lifetime computed by using different EOS and plotted as a function of ambient pressure and temperatures. Here, the droplet lifetime is defined when the nondimensional droplet surface area reaches a value of 0.2, and it is normalized by using a characteristic time as d_o^2/β, where d_o is the initial diameter, and β is the vaporization

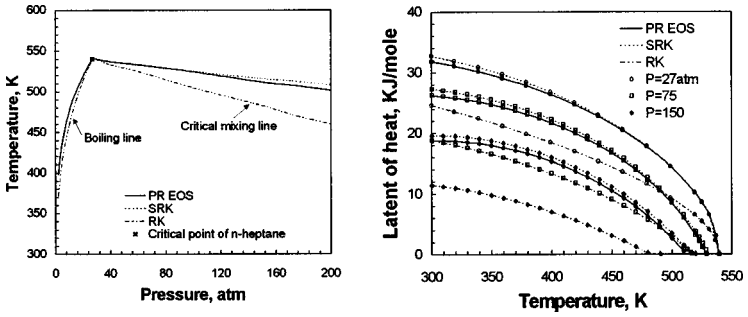

Fig. 2 (*a*) Phase equilibrium in terms of the pressure-temperature diagram and (*b*) latent heat of vaporization of n-heptane versus temperature for n-heptane-nitrogen system in thermodynamic equilibrium, as predicted by PR, SRK, and RK-EOS at three different pressures. See Fig. 1 for additional details.

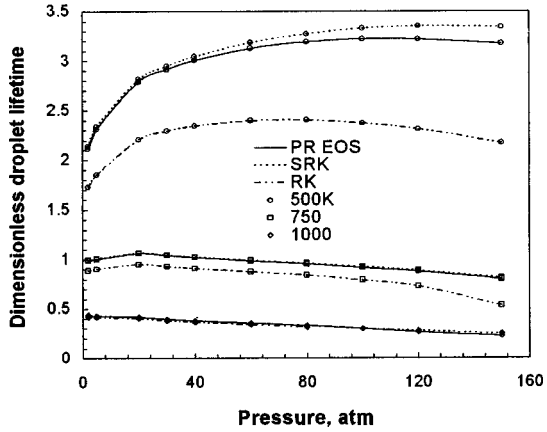

Fig. 3 Non-dimensional droplet lifetime, predicted by PR, SRK, and RK-EOS, plotted versus pressure at three different ambient temperatures

constant computed at $p=1$ atm and $T_a=750$ K. At high ambient temperatures, the droplet lifetime decreases monotonically as the ambient pressure is increased. However, at low to moderate ambient temperatures, the droplet lifetime first increases and then decreases as the ambient pressure is increased. This behavior is consistent with the reported experimental results ([18]), and can be explained as follows:

An increase in ambient pressure leads to the following effects: (i) the droplet heatup time increases and becomes a more significant part of droplet lifetime, since the fuel boiling temperature increases continuously with pressure until the droplet surface reaches a critical state, see Fig. 2(*a*); (ii) the mass transfer number *B*, which is generally expressed as $B=c_p\cdot(T_a-T_s)/L$, decreases as p is increased, since T_s increases with pressure; and (iii) the latent heat of vaporization (L) decreases and goes to zero as the droplet surface reaches a critical mixing point, see Fig. 2(*b*). At low to moderate ambient temperatures, the first two effects dominate, and, consequently, the droplet lifetime increases with pressure. At higher pressures, however, the third effect becomes dominant, since the heat of vaporization decreases drastically and goes to zero at the critical mixing point. Consequently, as indicated in Fig. 3 for ambient temperatures of 500 and 750 K, the droplet lifetime decreases with pressure at high pressures. Also, when the ambient temperature is sufficiently high, the first two effects become relatively less sensitive to pressure compared with the third effect, and the droplet lifetime decreases continuously as the ambient pressure is increased. These results also imply that the lifetime of a combusting droplet would decrease monotonically with increasing ambient pressure. This observation is well corroborated by experimental studies ([20]).

The sensitivity of the computed droplet lifetime to different EOS is also illustrated in Fig. 3. For all the cases examined, the lifetime predictions using PR-EOS and SRK-EOS are in good agreement with each other, except for small differences at low ambient temperatures ($T=500$ K) and at high pressures ($p>60$ atm). In contrast, at moderate ambient temperatures ($T_a=750$ K), RK-EOS significantly underpredicts the droplet lifetime compared with those obtained by using PR and SRK-EOS. This can be attributed to the fact that for given ambient temperature and pressure, RK-EOS predicts higher fuel vapor mole fraction at the droplet surface and lower heat of vaporization compared with those predicted by PR and SRK-EOS, see Figs. 1 and 2(*b*). At high ambient temperatures, however, the differences in the lifetime predictions using the three EOS are insignificant. This implies that the predicted gasification behavior of a combusting droplet may not be very sensitive to the particular EOS used.

Figure 4 shows the final temperature and fuel vapor mass fraction at the droplet surface plotted versus the ambient pressure.

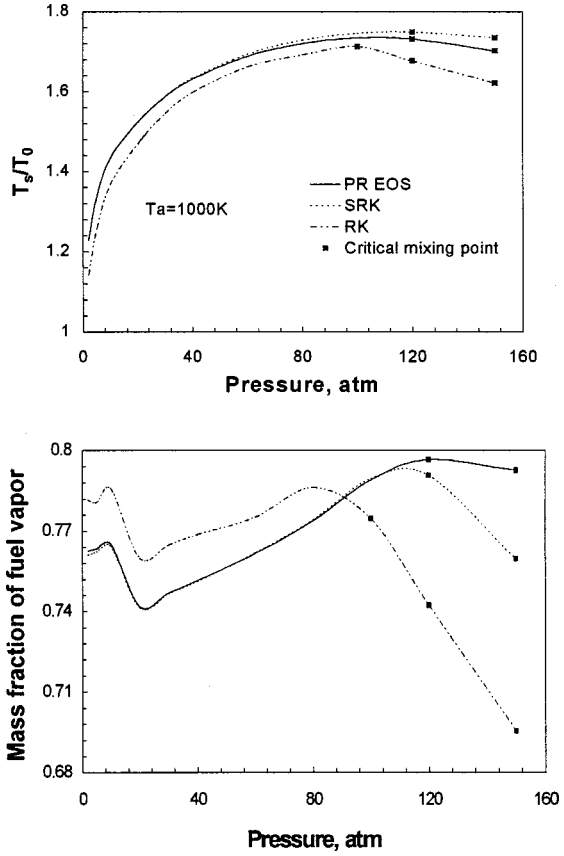

Fig. 4 Final temperature and fuel vapor mass fraction at the droplet surface plotted as functions of pressure. The ambient temperature (T_a) is 1000 K, and initial droplet temperature (T_o) 300 K. The final time corresponds to a time when $(d/d_o)^2=0.2$.

Again, the predictions of SRK and PR-EOS are in close agreement with each other over a wide pressure range, except for small deviations after the droplet surface reaches the critical mixing state. The predicted droplet surface temperature using RK-EOS is lower than that predicted by the other two EOS. More importantly, the predicted fuel vapor mass fraction using RK-EOS is higher compared to those obtained by using SRK and PR-EOS prior to the attainment of critical state and lower after the critical state. This is consistent with the phase-equilibrium results presented in Fig. 1, which indicates higher fuel vapor mass fraction for RK-EOS. The results for $P_r=5.0$ in Fig. 1 also indicate that with RK-EOS, the critical mixing point is attained at a lower temperature compared to that with the other two EOS. After the critical mixing point, the final temperature and fuel vapor mass fraction at the droplet surface decrease as the pressure is increased. This behavior is consistent with the phase-equilibrium results shown in Fig. 2(*a*), which indicates that the critical temperature decreases with critical pressure, as well as with those reported by Shuen et al. [12] and Jia and Gogos [14].

The literature indicates a wide scatter in the minimum ambient pressure required for attaining a critical mixing state at the droplet surface. Clearly, a reliable supercritical droplet gasification model should provide an accurate value of this pressure. As indicated in Fig. 4, at an ambient temperature of 1000 K, the minimum ambient pressure predicted by using PR and SRK-EOS is 120 atm ($P_r=4.44$), while that by using RK-EOS is 100 atm ($P_r=3.70$).

Figure 5 shows a comparison between our predictions and the measurements of Nomura et al. [21]. Results are presented in terms of the temporal variation of nondimensional surface area

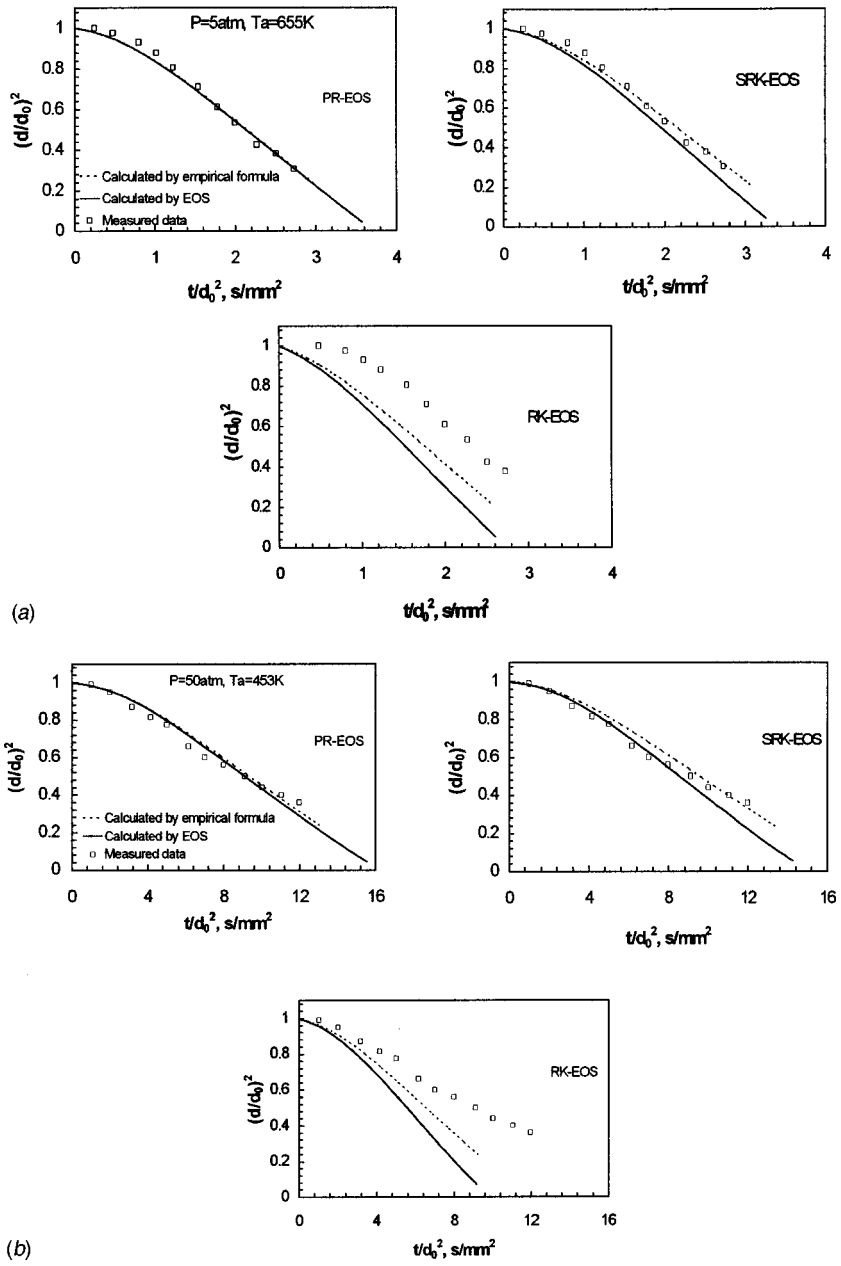

Fig. 5 (*a*) **Comparison between the predictions using PR, SRK, and RK-EOS and the measured data of Nomura et al. [21] at $P=5$ atm and $Ta=655$ K.** (*b*) **comparison between the predictions using PR, SRK, and RK-EOS and the measured data of Nomura et al. [21] at $P=50$ atm and $Ta=453$ K.**

obtained by using the three EOS for two different ambient conditions. In order to examine the effect of liquid density on predictions, the computed results are shown for two cases. An important observation is that using PR-EOS, the simulations reproduce experimental results quite well over a wide range of pressures. The numerical results obtained by using SRK-EOS are also in good agreement with experimental data, while those obtained by using RK-EOS exhibit significant differences, especially for the high-pressure case. Consistent with the earlier discussion, the RK-EOS significantly overpredicts the vaporization rate. For example, for $p=50$ atm and at a nondimensional time of 8, the numerical model based on RK-EOS predicts a nondimensional surface area of 0.2 compared to the experimental value of 0.6. The predictions of RK-EOS show improvement when the liquid density is calculated by the empirical formula, but still deviate noticeably from the experimental data.

In order to examine the supercritical droplet vaporization phenomena, we plot some important gas and liquid-phase properties during the transcritical state. Figure 6 shows the temporal variation of droplet surface area, surface temperature and liquid temperature at the droplet center for an ambient pressure of 120 atm. The predictions are based on PR-EOS with liquid density calculated by using the empirical formula. As indicated, the droplet surface, which is initially at a subcritical state, reaches the critical mixing state during later part of droplet lifetime. Furthermore, as the ambient temperature is increased, the surface temperature rises

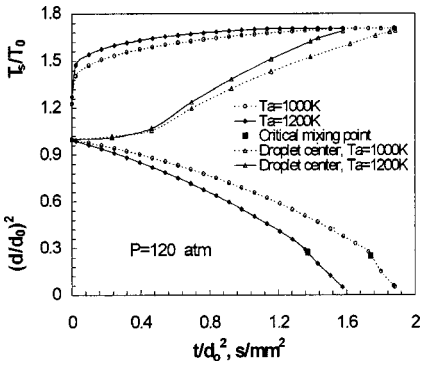

Fig. 6 Supercritical vaporization behavior in terms of the temporal variation of nondimensional droplet surface area, surface temperature and liquid temperature at the droplet center as predicted by PR-EOS

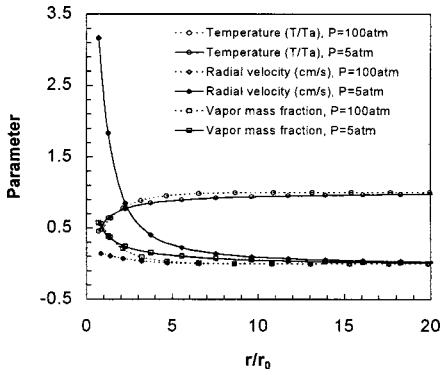

Fig. 8 Radial distribution of gas temperature, velocity, and fuel vapor mass fraction in the gas-phase region as predicted by PR-EOS for ambient pressures of 5 and 150 atm

at a faster rate, and the droplet surface reaches the critical mixing state earlier in droplet lifetime.

When the droplet surface approaches the critical mixing state, the difference between the gas and liquid phases disappears. In the present model, it is assumed that once the surface reaches the critical mixing state, it is maintained at that state. Note, however, that the critical mixing state varies with ambient temperature and pressure. The velocity of the critical mixing surface moving inwards to the droplet center then determines the vaporization rate. This velocity depends on how fast the inner liquid layer adjacent to the droplet surface attains the critical mixing temperature, which in turn depends on the distributions of liquid-phase properties within the droplet. It is also important to note that our simulations did not indicate any anomalous behavior during the transcritical stage of droplet evaporation.

In order to examine the multicomponent behavior of a pure fuel droplet at high pressure, we plot in Fig. 7 the radial distribution of liquid temperature and dissolved nitrogen within the droplet during different stages of droplet lifetime. The ambient conditions are the same as those in Fig. 6. As expected, the liquid nitrogen mass fraction has its maximum value at the droplet surface, and increases continuously with time until the droplet surface reaches a critical mixing state. Note that the critical mixing state for this case is attained at a nondimensional time of 0.69. This plot demonstrates that a pure fuel droplet evaporating in a supercritical environment exhibits multicomponent behavior. It is also noteworthy that while the liquid nitrogen mass fraction drops rapidly to a negligible value within a thin layer near the surface, the liquid temperature shows a more gradual decrease. This is indicative of small liquid mass diffusivity (relative to thermal diffusivity) or high liquid Lewis number.

Figure 8 shows the radial distribution of gas temperature, velocity, and fuel vapor mass fraction in the gas-phase region at two different ambient pressures. For these results, the PR-EOS has been employed. An important observation is that the radial distance over which the gas-phase properties vary significantly decreases as the ambient pressure is increased. For example, it decreases from ten to four times the droplet radius as the pressure is increased from 5 to 150 atm. This implies that the rates of heat and mass transport are enhanced, and, consequently, the vaporization rate is increased at higher pressures. It can be seen that the maximum gas velocity decreases dramatically when the pressure is increased from 5 to 150 atm, which also implies a change in the gas-phase unsteadiness.

The literature indicates a wide scatter in the minimum ambient pressure required for a droplet to attain a critical mixing state at its surface. Clearly, this value depends on several liquid and gas-phase properties including ambient temperature and composition, initial droplet diameter, and liquid fuel properties. Figure 9 shows the minimum ambient pressure as a function of ambient temperature. In order to obtain this minimum pressure value, simulations were performed for increasingly higher pressures, but at fixed ambient temperature, until a critical mixing state is observed at the droplet surface. The plot in Fig. 9 represents a boundary (in terms of the ambient temperature and pressure) between the subcritical and supercritical vaporization. Any point above the curve indicates that a critical mixing state will be reached sometime during the droplet lifetime, or the droplet will undergo transcritical evaporation during its lifetime. On the other hand, any point below the curve implies that the droplet is not likely to attain a supercritical state during its lifetime. Also, farther a point is from the curve (in the supercritical region), earlier in its lifetime does the droplet reach the critical mixing state.

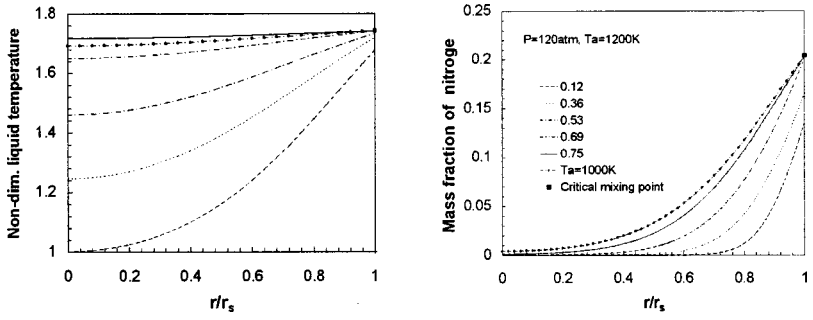

Fig. 7 Radial distribution of liquid temperature (*a*) and dissolved nitrogen (*b*) in the droplet interior at different stage of droplet lifetime, as predicted by PR-EOS. The number for each curve represents a fraction of droplet lifetime.

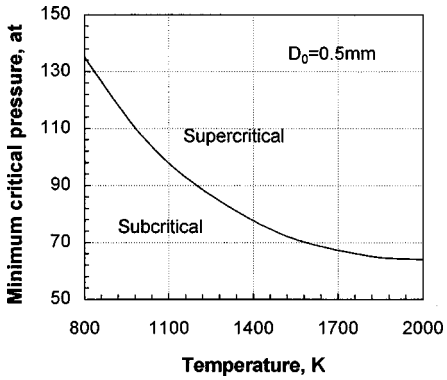

Fig. 9 Minimum pressure, required for an n-heptane fuel droplet to attain a critical mixing state, plotted as a function of ambient temperature

Conclusions

In this paper, the transcritical droplet vaporization phenomena has been investigated. The computational model considers the transient, spherically symmetric conservation equations for gas and liquid phases, pressure-dependent variable thermophysical properties, and a detailed treatment of the liquid-vapor phase equilibrium at the droplet surface. The model is shown to reproduce the subcritical, transcritical, and supercritical vaporization behavior of a liquid fuel droplet over a wide range of ambient conditions. In addition, the effects of using different EOS on predicting the equilibrium composition and transcritical droplet vaporization have been examined. Important observations are as follows:

1 For an n-heptane-nitrogen system, the phase-equilibrium predictions using RK-EOS show significant differences from those using PR and SRK-EOS. The RK-EOS yields higher fuel vapor concentration, higher solubility of nitrogen into liquid, lower critical-mixing-state temperature, and lower latent heat of vaporization compared to those obtained by using PR and SRK-EOS.

2 At low to moderate ambient temperatures, RK-EOS significantly overpredicts the droplet vaporization rate, and underpredicts the droplet lifetime compared to that using the other two EOS. Also, using RK-EOS, the critical mixing state at the droplet surface is reached earlier in droplet lifetime compared to that by using the other two EOS. These differences become less noticeable at higher ambient temperatures ($Ta \geqslant 1000$ K), implying that for a combusting droplet, differences in the predictions of three EOS may not be significant. The droplet lifetime predictions of PR-EOS are in excellent agreement with measurements ([21]) over a wide range of ambient pressures. In contrast, the predictions based on RK-EOS show significant differences with measurements, while those based on SRK-EOS are in reasonable agreement with measurements.

3 At low to moderate ambient temperatures, the predicted droplet lifetime first increases reaching a maximum value, and then decreases as the ambient pressure is increased. At high ambient temperatures ($Ta \geqslant 1000$ K), however, the droplet lifetime decreases monotonically with increasing pressure. These results are in agreement with the reported experimental and numerical results ([19–21]).

Acknowledgment

This work was partially funded by the GE Aircraft Engines.

Nomenclature

c_p = specific heat at constant pressure
h = enthalpy
H = partial molar enthalpy
I = internal energy
k = thermal conductivity
$\dot{m}$ = droplet vaporization rate
r = spatial variable
p = pressure
$r_s(t)$ = instantaneous droplet radius
R = gas constant
t = temporal variable
T = temperature
V = specific volume
ρ = mixture density
z = compressibility factor

Subscripts

k = gas species
l = liquid-phase property

References

[1] Manrique, J. A., and Borman, G. L., 1969, "Calculation of Steady State Droplet Vaporization at High Ambient Pressures," Int. J. Heat Mass Transf., **12**, pp. 1081–1095.
[2] Chueh, P. L., and Prausnitz, J. M., 1968, "Calculation of High Pressure Vapor-Liquid Equilibria," Ind. Eng. Chem., **60**, pp. 34–52.
[3] Savery, C. W., and Borman, G. L., 1970, "Experiments on Droplet Vaporization at Supercritical Pressures," AIAA Paper No. 70-6.
[4] Lazar, R. S., and Faeth, G. M., 1971, "Bipropellant Droplet Combustion in the Vicinity of the Critical Point," *Proc. 13th Symp. on Combustion*, The Combustion Institute, Pittsburgh, PA, pp. 801–811.
[5] Canada, G. S., and Faeth, G. M., 1973, "Fuel Droplet Burning Rates at High Pressures," *Proc. of 14th Symp. on Combustion*, The Combustion Institute, Pittsburgh, PA, pp. 1345–1354.
[6] Matlosz, R. L., Leipziger, S., and Torda, T. P., 1972, "Investigation of Liquid Drop Evaporation in a High Temperature and High Pressure Environment," Int. J. Heat Mass Transf., **15**, pp. 831–852.
[7] Curtis, E. W., and Farrell, P. V., 1988, "Droplet Vaporization in a Supercritical Microgravity Environment," Acta Astronaut., **17**, pp. 1189–1193.
[8] Curtis, E. W., and Farrell, P. V. A., 1992, "Numerical Study of High-Pressure Droplet Vaporization," Combust. Flame, **90**, pp. 85–102.
[9] Peng, D., and Robinson, D. B., 1976, "A New Two-Constant Equation of State," Ind. Eng. Chem. Fundam., **15**, pp. 59–64.
[10] Hsieh, K. C., Shuen, J. S., and Yang, V., 1991, "Droplet Vaporization in High Pressure Environments I: Near Critical Conditions," Combust. Sci. Technol., **76**, pp. 111–132.
[11] Graboski, M. S., and Daubert, T. E., 1987, "A Modified Soave Equation of State for Phase Equilibrium Calculations I: Hydrocarbon Systems," Ind. Eng. Chem. Process Des. Dev., **17**, pp. 443–337.
[12] Shuen, J. S., Tang, V., and Hsiao, C. C., 1992, "Combustion of Liquid-Fuel Droplets in Supercritical Conditions," Combust. Flame, **89**, pp. 299–319.
[13] Delplanque, J. P., and Sirignano, W. A., 1993, "Numerical Study of the Transient Vaporization of an Oxygen Droplet at Sub- and Super-Critical Conditions," Int. J. Heat Mass Transf., **36**, pp. 303–314.
[14] Jia, H., and Gogos, G., 1993, "High Pressure Droplet Vaporization; Effects of Liquid-Phase Gas Solubility," Int. J. Heat Mass Transf., **36**, pp. 4419–4431.
[15] Jia, H., and Gogos, G., 1992, "Investigation of Liquid Droplet Evaporization in Subcritical and Supercritical Gaseous Environments," J. Thermophys. Heat Transfer, **6**, pp. 738–745.
[16] Stengele, J., Bauer, H. J., and Wittig, S., 1996, "Numerical Study of Bicomponent Droplet Vaporization in a High Pressure Environment," Presented at the International Gas Turbine and Aeroengine Congress & Exhibition, Birmingham, UK, Paper No. 96-GT-442.
[17] Aggarwal, S. K., Shu, Z., Mongia, H., and Hura, H. S., 1998, "Multicomponent and Single-Component Fuel Droplet Evaporation Under High Pressure Conditions," AIAA Paper No. 98-3833.
[18] Faeth, G. M., 1977, "Current Status of Droplet and Liquid Combustion," Prog. Energy Combust. Sci., **3**, pp. 191–224.
[19] Givler, S. D., and Abraham, J., 1996, "Supercritical Droplet Vaporization and Combustion Studies," Prog. Energy Combust. Sci., **22**, pp. 1–28.
[20] Kadota, T., and Hiroyasu, H., 1982, "Combustion of a Fuel Droplet in Supercritical Gaseous Environments," *Proc. 18th Symp. on Combustion*, The Combustion Institute, Pittsburgh, PA, pp. 275–282.
[21] Nomura, H., Ujiie, Y., Rath, H. J., Sato, J., and Kono, M., 1996, "Experimental Study of High-Pressure Droplet Evaporation Using Microgravity Conditions," *Proc. 26th Symp. on Combustion*, The Combustion Institute, Pittsburgh, PA, pp. 1267–1273.
[22] Reid, R. C., Prausnitz, J. M., and Poling, B. E., 1987, *The Properties of Gases and Liquids*, McGraw-Hill, New York.
[23] Knapp, H., Doring, R., Oellrich, L., Plocker, U., and Prausnitz, J. M., 1982, "Vapor-Liquid Equilibria for Mixture of Low Boiling Substances," Chem. Eng. Data, Series, Vol. VI, DECHEMA, Frankfurt.
[24] Chung, T. H., Ajlan, M., Lee, L. L., and Starling, K. E., 1988, "Generalized Multiparameter Correlation for Nonpolar and Polar Fluid Transport Properties," Ind. Eng. Chem., **27**, pp. 671–679.

[25] Neufeld, P. D., Janzen, A. R., and Aziz, R. A., 1972, ''Empirical Equations to Calculate 16 of the Transport Collision Integrals $\Omega^{(l,s)}$ for the Lennard-Jones Potential,'' J. Chem. Phys., **57**, pp. 1100–1102.
[26] Takahashi, S., 1974, ''Preparation of a Generalized Chart for the Diffusion Coefficients of Gases at High Pressures,'' J. Chem. Eng. **6**, pp. 417–420.
[27] Bird, R. B., Stewart, W. E., and Lightfoot, E. N., 1960, *Transport Phenomena*, John Wiley and Sons, New York.
[28] Byung, I. L., and Michael, G. K., 1975, ''A Generalized Thermodynamic Correlation Based on Three-Parameter Corresponding States,'' AIChE J., **21**, pp. 510–527.
[29] Filippov, L. P., 1956, ''Thermal Conduction of Solutions in Associated Liquids: Thermal Conduction of 50 Organic Liquids,'' Chem. Abstr., **50**, Col. 8276.
[30] Nakanishi, K., 1978, ''Prediction of Diffusion Coefficients of Nonelectrolytes in Dilute Solution Based on Generalized Hammond-Strokes Plot,'' Ind. Eng. Chem. Fundam., **17**, pp. 253–256.
[31] Hankinson, R. W., and Thomson, G. H., 1979, ''A New Correlation for Saturated Densities of Liquids and Their Mixtures,'' AIChE J., **25**, pp. 653–663.
[32] Thomson, G. H., Brobst, K. R., and Hankinson, R. W., 1982, ''An Improved Correlation for Densities of Compressed Liquids and Liquid Mixtures,'' AIChE J., **28**, pp. 671–676.